# Surface adhesion and membrane fluctuations influence the elastic modulus of extracellular vesicles

Fredrik Stridfeldt,[1] Hanna Kylhammar,[1] Prattakorn Metem,[2] Vikash Pandey,[3] Vipin Agrawal,[3] Andre Görgens,[4,5,6] Doste R. Mamand,[4,5] Oskar Gustafsson,[4,5] Samir El Andaloussi,[4,5] Dhrubaditya Mitra,[3] and Apurba Dev[1,7]

[1] *Department of Applied Physics, KTH Royal Institute of Technology, Stockholm, Sweden*
[2] *Division of applied electrochemistry, KTH Royal Institute of Technology, Stockholm, Sweden*
[3] *Nordita, KTH Royal Institute of Technology and Stockholm University, Stockholm, Sweden*
[4] *Department of Laboratory Medicine, Division of Biomolecular and Cellular Medicine, Karolinska Institutet, Stockholm, Sweden*
[5] *Department of Cellular Therapy and Allogeneic Stem Cell Transplantation (CAST), Karolinska University Hospital Huddinge and Karolinska Comprehensive Cancer Center, Stockholm, Sweden*
[6] *Institute for Transfusion Medicine, University Hospital Essen, University of Duisburg-Essen, Essen, Germany*
[7] *Department of Electrical Engineering, Uppsala University, Uppsala, Sweden*

Elastic properties of nanoscale extracellular vesicles (EVs) are believed to influence their cellular interactions, thus having a profound implication in intercellular communication. Yet, an accurate quantification of the elasticity of such small lipid vesicles is difficult even with AFM-based nanoindentation experiments as it crucially depends on the reliability of the theoretical interpretation of such measurements. We developed here a unified model and experimental procedure to reliably estimate the elastic modulus of EVs. Further, we experimentally demonstrate that the quantification of EV-elastic modulus from AFM-based force spectroscopy measurement is marred by the interplay of their compositionally inhomogeneous fluid membrane with the adhesion forces from the substrate and thermal effects, two exquisite phenomena which could thus far only be theoretically predicted. The effects result in a large spreading of elastic modulus even for a single EV. Our unified model is then applied to genetically engineered classes of EVs to understand how the alterations in tetraspanin expression may influence their elastic modulus.

## I. INTRODUCTION

The discovery of EVs and their numerous roles in pathophysiological processes are in many ways redefining our approaches and understanding of human health and diseases[1, 2]. Released to the extracellular milieu by most cell types, these nanovesicles carry a wide variety of cellular components including proteins, nucleic acids, and lipids, and are known to deliver their bioactive cargo to a recipient cell, thereby, inducing functional alterations [3]. During the past decade, this topic has generated exploding interest, consequently driving countless technical innovations. While these efforts have helped to overcome many of the initial challenges and skepticism, the high heterogeneity of EVs even when they are released by a single cell has triggered the obvious questions; are there EV subpopulations in circulation that are functionally differential or more relevant than others? If so, which property is the best indicator of such functional differences?

While a single EV approach is arguably the best way to address such heterogeneity, given their nanoscale dimension and diverse molecular repertoire, existing techniques can not perform a comprehensive chemical analysis at a single vesicle. Thus far, optical/fluorescence techniques have been the main methods to interrogate single EVs, although providing only a limited set of information [4, 5]. In this context, the recent attempts made with atomic force microscopy (AFM) has brought renewed enthusiasm as it can provide complementary information, e.g. stiffness, bending modulus, adhesion etc. [6]. Given the stiffness of EVs may influence their cellular uptake, the topic has also larger implications concerning EV biology and functions [7].

However, being enclosed with a compositionally inhomogeneous fluid-like lipid bilayer, EVs offer yet unexplored challenges for nanoindentation-based measurements, as well as avenues to study some fundamental nature of lipid bilayer which could only be predicted from theory so far. Two such effects are also likely to have significant influence on the membrane elasticity are: (i) the competition between adhesion and shape deformation leading to a different mechanism of tether formation for surface adhered vesicles [8, 9], which is the case for most EV studies with AFM and (ii) the effect of membrane fluctuations on the elastic property [10]. To what extent do these effects influence the elastic modulus of EVs remain unknown and so is the accuracy of the previous attempts [11, 12] to quantify the elastic modulus of EVs. Besides, it is also unknown if the alteration in the membrane protein composition can induce measurable changes in EV elasticity.

Here we apply the Canham-Helfrich model (CH model), which has been extensively used to understand force spectroscopy of Giant Unilamellar Vesicles (GUVs) [13], to quantify the elastic properties of EVs from force spectroscopy. We find that in contrast to previous reports [11], the EVs behave as surface-adhered vesicles showing a linear dependence of tether force on the tether length. We then apply our method to different EV populations derived from the human embryonic kidney (HEK293T) cell line and its genetically engineered versions with altered tetraspanins expression. The bending modulus estimated for the different EV families range

from $15.7 - 33.0\,\mathrm{k_B T}$ with large fluctuations within each family of vesicles which is consistent with inherent EV heterogeneity. Interestingly, our experiments also show large fluctuations of measured values even for a *single EV* when repeatedly examined under identical conditions. We suggest that such behavior is driven by both thermal and compositional effects, as expected for such nanoscale objects. We find that the probability distribution function (PDF) of elastic moduli are best described by not a single Gaussian but superposition of Gaussians. Consequently, commonly used techniques to test for statistical significance, e.g., the student's t-test can not be employed. We use Jensen-Shanon divergence to differentiate between the PDFs. Our results suggest that protein alternations might have an influence on the elastic moduli of EVs, but they are often hidden in such large fluctuations.

## II. RESULTS

We performed force spectroscopy in a liquid environment (1×PBS) on EVs derived from HEK293T cell line We followed the isolation method as described in our previous article [14]. To assess the influence of protein alterations on the elastic properties of EVs, the expression of tetraspanins was genetically altered in the cell producing two different classes of EVs along with the wild type (WT-EVs): (i) sample with CD63 knockout (CD63-KO) and (ii) sample with CD63-CD81-CD9 knockout (Pan-KO). To assess the effect of protein corona, if any, we analyzed an additional sample type referred to as WT-SEC. To remove the protein corona, we followed an earlier report [15], and further processed WT-EVs with bind-elution size exclusion chromatography. For more details regarding the sample preparation, see IV C.

### A. Shape of adhered vesicles

A typical topographical profile for an EV measured by AFM in a liquid environment is shown in Fig. (1A). Theories and experiments of adhesion of GUVs to glass cover slips [16–18] suggest that the shape of the vesicle would be that of a spherical cap. Earlier works [6, 19] on nano-vesicles have also made the same assumption. The topographical profile is a height field $H$ as a function of two-dimensional coordinates $x$ and $y$, typical examples are shown in Fig. (1B). The height field as a function of the slow axis of the scanning of the AFM – along the lines marked in Fig. (1B) – is shown in Fig. (1C). We fit a circle to this profile taking into account the correction due to the shape of the tip of the AFM to determine the effective radius ($R_\mathrm{c}$) of the EV, as earlier described in Ref. [19]. We show in Fig. (1C) the measured height, its fitted arc, and the tip-corrected EV shape for a typical example. The probability distribution of the ratio $H/R_\mathrm{c}$ for all the vesicles is presented in Fig. (1D). A vesicle with $H/R_\mathrm{c} > 2$ indicates a non-realistic shape and was disregarded from future analysis. The radius $R_\mathrm{c}$ ranges from approximately 40 nm to 100 nm. Almost all of them fall within the class of small EVs(sEV) defined [see e.g., 20, page 9] to be less than 200 nm in diameter but few are not. Hence in the rest of this paper, we call them EVs.

For the measurement of force–distance curves, care is necessary. The EVs need to be immobile for the entire process, and the applied tip force and tip velocity must be small enough to not cause irreversible damage to the EVs. Any data we used in the following analyses were extracted sufficiently far away from the coverslip to avoid influence by any substrate effects. We image every EV twice – before and after the force spectroscopy – to make sure they are not damaged or have moved, see Fig. (1B) and Fig. (1C). In total, we imaged and performed force-spectroscopy on 49 vesicles of the WT family 39 of the WT-SEC family, 24 of CD63-KO family, and 18 of the Pan-KO family.

### B. Force–distance measurements

In Fig. (2A) we show a typical example of the force–distance curves. Here we plot only the approach curve. As we repeat the experiment many times ($\gtrsim 150$) on the same EV, each time we obtain a different force–distance curve. The spread is not originating from the setup, as can be seen by plotting the same experiment but on a clean coverslip instead of an EV, see (Appendix 7). This large variation in the force–distance curves is not seen in GUVs. We shall revisit this aspect later. The average of all the force–distance curves is shown in red. We shall call this the *average* force–distance curve.

#### *1. Theory*

The EVs are similar to Giant Unilamellar Vesicles (GUVs) in the sense that both are a drop of fluid enclosed within a lipid bilayer[21]. The two essential differences are: (i), the membrane of the EVs contain many other molecules, including proteins and cholesterol; and (ii), the EVs are much smaller in size. Hence we expect that the theory that describes the force–distance curves of EVs is similar to the theory applied to GUVs. Next, we present a summary of our theory – a more detailed description can be found in (Appendix B).

1. Typically, the force–distance experiments on cells, e.g., red blood cells (RBCs) are interpreted with Hertzian contact mechanics [22–25]. Within this model, the cell is a deformable *solid*. At small distance $d$, the force $F$ is given by $F \propto d^{3/2}$. The EVs cannot be modeled as solids because they lack the internal organelles and cytoskeleton of the cell.

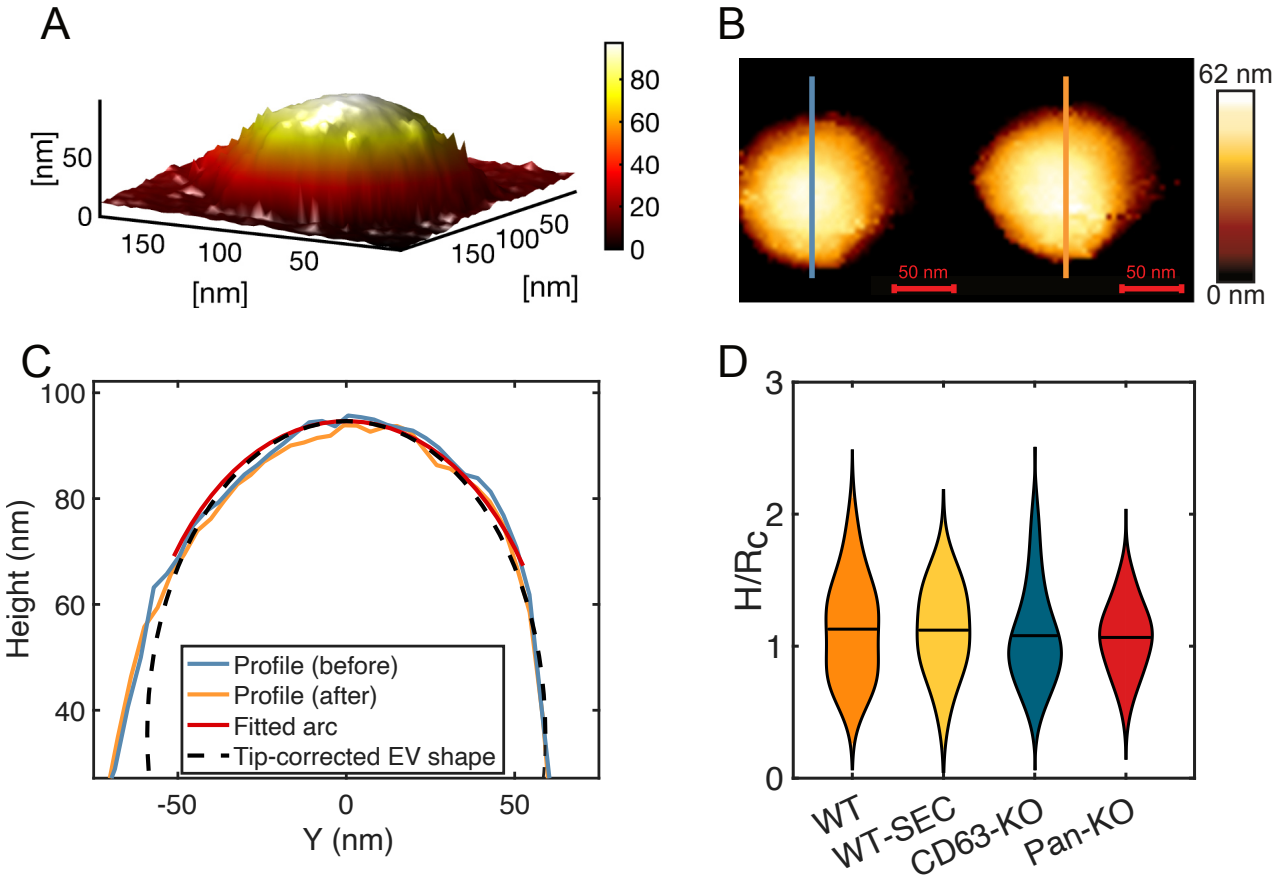


FIG. 1. **Topographic image** (A) Topographic image of a single vesicle. (B) The height field plotted as a color for a typical vesicle before (left) and after (right) force spectroscopy. (C) The measured height, its fitted arc, and the tip-corrected EV shape extracted from the line shown in (B). (D) The ratio of the height and the radius of curvature. The horizontal black line indicates mean of the ratio. Mean for WT: 1.13, WT-SEC:: 1.12, CD63-KO: 1.08, and Pan-KO: 1.07.

2. The lipid bilayer (with the addition of proteins, nucleic acids, and glycans) of EVs is a (two-dimensional) fluid. It has zero shear modulus but a non-zero area modulus $K_{\mathrm{A}}$. The usual thin–shell theory [22, 26, 27], which has also been generalized to pressurized shells [10, 28], includes (in–plane) shear modulus and is therefore not applicable to EVs. In other words, the shell in standard thin–shell–theory is a two–dimensional solid whereas the bilipid membrane of EVs is a two–dimensional fluid.

3. Thus, the EVs must be modeled as shells but with fluid membranes, similar to the model of GUVs. We call this the Canham-Helfrich model. In this model, a deformation contributes to the change in energy in three possible ways: change in area, change in volume, and change in curvature or bending. Henceforth we use this model to interpret the force–distance curves.

Assuming that a reasonable estimate of the bending modulus of EVs is the typical bending modulus of lipid bilayers, it is possible to show that the contribution of bending to the change in curvature is very small [6]. Following the standard prescription for GUVs [13] we assume that the volume of the vesicle remains unchanged. This is justified because the only way the volume can change is if water leaks out of the semi-permeable membrane. Using existing data for the permeability of water through bilipid membranes, we find that within the time scale of the experiment the leakage is negligible – the volume remains constant, see (Appendix B 3). Then the only possibility that remains is the change in area.

Let us consider the case where a small external force $F$ generates a small deformation $d$. Let $R_{\mathrm{v}}$ be the effective radius of the vesicle defined by $(4/3)\pi R_{\mathrm{v}}^3 \equiv V$, where $V$ is the volume of the adhered vesicle. We consider $d \ll R_{\mathrm{v}}$ such that $d/R_{\mathrm{v}}$ is a small parameter. Then the change in free–energy can be estimated as (Appendix B 1)

$$\Delta\mathcal{F} \approx B_1 K_{\mathrm{A}} d^2 - B_2 F d \tag{1}$$

where $B_1$ and $B_2$ are dimensionless constants that depend on the details of the indentor and the shape of the adhered vesicle and $K_{\mathrm{A}}$ is the in–plane area modulus of the membrane. The second term in the free energy is the

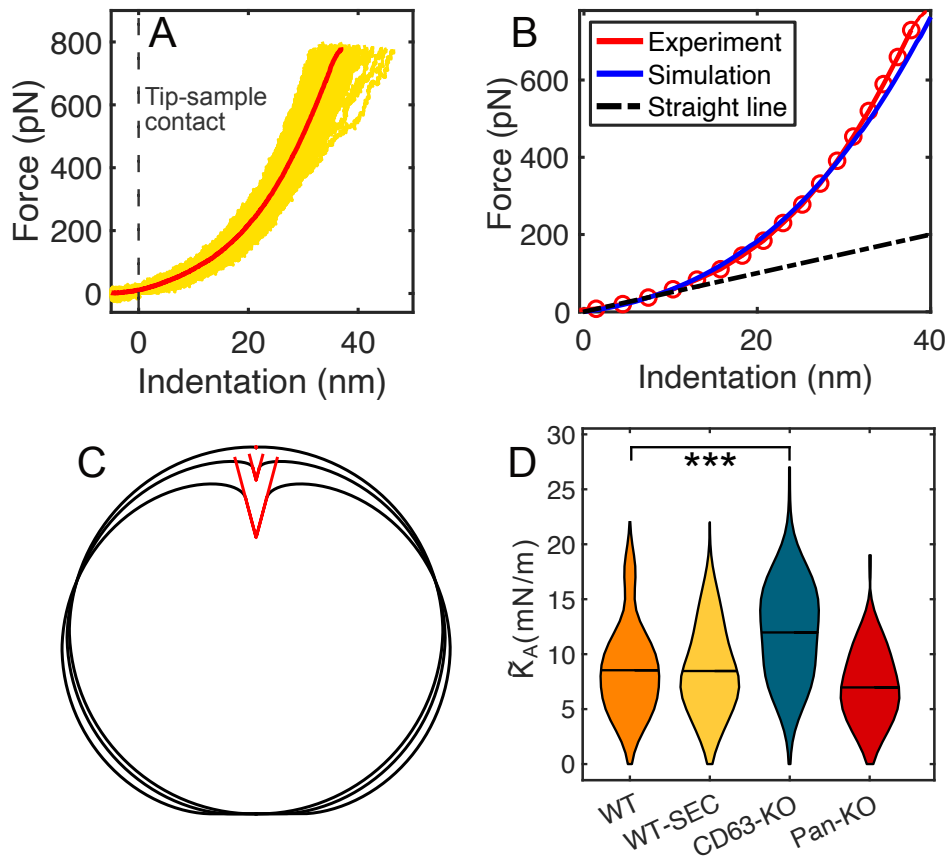


FIG. 2. **Approach curves** (A) 150 indentation iterations on a vesicle (yellow lines). The average force–distance curve is shown in red. (B) The average indentation curve from (A), and the curve subject to the fitting of the model for $K_A = 618.84\,\mathrm{mN\,m^{-1}}$ and $\Sigma_0 = 5.49\,\mathrm{mN\,m^{-1}}$ in the same scale. The dashed black line shows a linear fit at small distances. (C) The shape of the vesicle obtained from our simulations for three different values of the force $F = 2, 90, 600$ pN respectively. The red triangle illustrates the conical tip with the half-cone angle of 15. (C) The probability distribution function, plotted as a violin plot, of the $\tilde{K}_A$ of vesicles from the different families: WT, WT-SEC, CD63-KO, and Pan-KO. These are calculated from the *average* force–distance plots for each vesicle. The horizontal black line indicates the mean.

work done by the indenting force. The formula assumes that the $d$ is so small that it does not significantly change the adhesion energy of the EV to the bottom plate. Minimizing the free–energy with respect to $d$ and setting it to zero we obtain $F \propto K_A d$ – a linear force–distance relationship. Note that thin–shell–theory for pressurized shells also gives a linear force–distance relationship for small deformation [10, 28].

Unfortunately, the linear force–distance relationship for small deformation does not allow us to determine the elastic modulus $K_A$ because the constant of proportionality, which depends on the adhered shape of the vesicle and the geometry of the indentor, can not be determined by the kind of dimensional arguments given here. Nevertheless two vesicles with exactly the same surface molecules would have exactly the same interaction with the coverslip and in all cases we have used the AFM probe with the same geometry, hence we can define an effective elastic modulus $\tilde{K}_A$ from the slope of the force–distance curve at small deformation. Although this approach does not allow us to measure the $K_A$ accurately, it does allow us to measure *the change* in $K_A$ as a result of knocking out of certain proteins. In Fig. (2B) we show a typical example of the average force–distance curve (blue line) together with a linear fit at small distances. The slope of the straight line gives $\tilde{K}_A$.

To fit the force–distance curve over a larger range we need numerical simulations. We follow Ref. [29] who solved the same problem for GUVs, see also (Appendix B 2). Again the only free–energy cost that comes from defomation is due to change in area – the volume is assumed to be constant. The adherence of the vesicle is modeled by a pre–stress, $\Sigma_0$. By obtaining the best fit of the numerical solution of the model to the experimental data we obtain the two fit parameters, $K_A$ and $\Sigma_0$. A typical example is shown in Fig. (2B). The numerical and the experimental force–distance curves agree well with each other not only at short distances but over almost the complete range of distances.

### 2. Experiments

Returning to the experiments we plot the *average* force–distance curve for a single vesicle in Fig. (2B). We find that there is indeed a small range of scale over which $F \propto d$. As the indentation progresses the response becomes nonlinear. We also note the agreement between the simulation and the experiment. Next, we fit a straight line to the first 10% of the indentation (roughly equal to 50 data points) of every indentation's force–distance curve. The slope of the straight line gives the effective modulus $\tilde{K}_{\mathrm{A}}$ for each vesicle. The probability distribution functions (PDFs) of the average effective modulus $\tilde{K}_{\mathrm{A}}$ of the families are plotted in Fig. (2D) as violin plots. The mean and standard deviation of the $\tilde{K}_{\mathrm{A}}$ of the samples are $8.5\,\mathrm{mN\,m^{-1}}$ and $3.9\,\mathrm{mN\,m^{-1}}$ for the WT family, $8.5\,\mathrm{mN\,m^{-1}}$ and $3.7\,\mathrm{mN\,m^{-1}}$ for WT-SEC, $12.0\,\mathrm{mN\,m^{-1}}$ and $3.8\,\mathrm{mN\,m^{-1}}$ for CD63-KO, and $7.0\,\mathrm{mN\,m^{-1}}$ and $2.8\,\mathrm{mN\,m^{-1}}$ for Pan-KO, respectively. In comparison to the WT family, vesicles shedded by CD63-KO cells have a higher mean $\tilde{K}_{\mathrm{A}}$ while the Pan-KO family shows a lower mean $\tilde{K}_{\mathrm{A}}$. We test the significance of these differences using unpaired two-sample t-tests and find $P \approx 5 \times 10^{-4}$ when comparing the means of the WT and CD63-KO families. No other family shows a statistical deviation in the mean when compared to the WT family ($P > 0.05$). Earlier studies [30–32] have reported similar effective elastic moduli of various EVs ranging from $7\,\mathrm{mN\,m^{-1}}$ up to $49\,\mathrm{mN\,m^{-1}}$. These studies have all extracted the moduli in a similar way and on similar sample sizes. We have not found any earlier nanomechanical studies on EVs derived from HEK293T cells. Besides, the influence of protein alterations has not been studied to the best of our knowledge.

The nature of the PDFs plotted in Fig. (2D) suggests that they cannot be approximated by a single Gaussian. This is confirmed by the negative result of the Shapiro–Wilk test, see (Appendix C). In fact, we calculate the PDFs using kernel density estimation with a Gaussian kernel. In other words, we find the superposition of Gaussian distributions that best fit our data. In (Appendix E), we plot both the histograms and the PDFs estimated by the kernel density estimation for all the families.

## C. Variation of area modulus

The PDFs show the inherent heterogeneity of the deformability of the EVs coming from all the different sample families. While the WT, WT-SEC, and Pan-KO families resemble each other in distribution shape, peak, and mean, the CD63-KO distribution shows deviations from the rest. Are the differences we see statistically significant? As the PDFs are not simple Gaussians, the student's t-test can not be employed here to test the statistical significance [33]. Hence we need to use a technique that does not assume simple Gaussianity. Furthermore, note that we are dealing with small sample sizes in each family, hence the PDFs themselves are poorly determined. Next, remember that the effective elastic modulus $\tilde{K}_{\mathrm{A}}$ was determined by a linear fit to the *average of all force–distance curves* of a single vesicle but the force–distance curves of a single vesicle show large variation. Thus there are additional sources of error to be taken into account. Let us fit a straight line (at small distances) to the individual force–distance curves for a single vesicle to calculate a $\tilde{K}_{\mathrm{A}}$ for each force–distance curve. Hence for a single vesicle, we obtain about 150 values of $\tilde{K}_{\mathrm{A}}$. We plot them in Fig. (3A). The values are close to normally distributed but show significant variation, see also (Appendix 8). Note that these values are decorrelated with one other. In Fig. (3B) we present the range of values of $\tilde{K}_{\mathrm{A}}$ that we obtain from individual force–distance curves for each of the families in barcode plots. The families WT and WT-SEC are close to each other although the former shows a larger span of $\tilde{K}_{\mathrm{A}}$ values. The family CD63-KO has relatively high values of $\tilde{K}_{\mathrm{A}}$ compared to the WT and the family Pan-KO seems to have relatively smaller values of $\tilde{K}_{\mathrm{A}}$ compared to WT. At this stage, we consider for each family three PDFs of $\tilde{K}_{\mathrm{A}}$ in the following manner. Let the average $\tilde{K}_{\mathrm{A}}$ for a single vesicle be denoted by $\left\langle \tilde{K}_{\mathrm{A}} \right\rangle$, and its standard deviation $\Delta\tilde{K}_{\mathrm{A}}$. Then we have one PDF each for $\left\langle \tilde{K}_{\mathrm{A}} \right\rangle - \Delta\tilde{K}_{\mathrm{A}}/2$, $\left\langle \tilde{K}_{\mathrm{A}} \right\rangle$, and $\left\langle \tilde{K}_{\mathrm{A}} \right\rangle + \Delta\tilde{K}_{\mathrm{A}}/2$, we denote them respectively by $\mathcal{P}_1$, $\mathcal{P}_2$ and $\mathcal{P}_3$. In Fig. (3C) we show that for the WT family. A way to measure the distance between any two PDFs, $p(x)$ and $q(x)$ is to calculate their Jensen–Shanon divergence [34] defined by

$$D_{\mathrm{JS}} \equiv \frac{1}{2}\left[D_{\mathrm{KL}}\left(p \,\middle|\, \frac{p+q}{2}\right) + D_{\mathrm{KL}}\left(q \,\middle|\, \frac{p+q}{2}\right)\right] \tag{2a}$$

$$\text{where} \quad D_{\mathrm{KL}}\left(p \,\middle|\, q\right) \equiv \int dx p(x) \log\left(\frac{p(x)}{q(x)}\right). \tag{2b}$$

Here $D_{\mathrm{KL}}$ is the well-known Kullback–Leiber divergence. We measure the Jensen–Shanon divergence between $\mathcal{P}_1$ and $\mathcal{P}_3$ of one family and between $\mathcal{P}_2$ of two families and plot them as a matrix in Fig. (3D). The 11 element of this matrix is the $D_{\mathrm{JS}}$ between $\mathcal{P}_1$ and $\mathcal{P}_3$ for the WT family. Similarly, all the diagonal elements show the same distance for each family. The off-diagonal elements show the distance between the $\mathcal{P}_2$ of two different families. By looking at the first column (or row) of this matrix we see that for the WT family, the distance within the family is much more than the distance between this family and any other family. There is only one case where the distance within the family is less than the distance between the families – compare CD63-KO with Pan-KO. The distance between $\mathcal{P}_1$ and $\mathcal{P}_2$ within CD63-KO family is 0.2 whereas the distance between $\mathcal{P}_2$ of CD63-KO family with Pan-KO family is 0.24. This is the only case where we may claim that our method distinguishes one family from another, even then the difference between

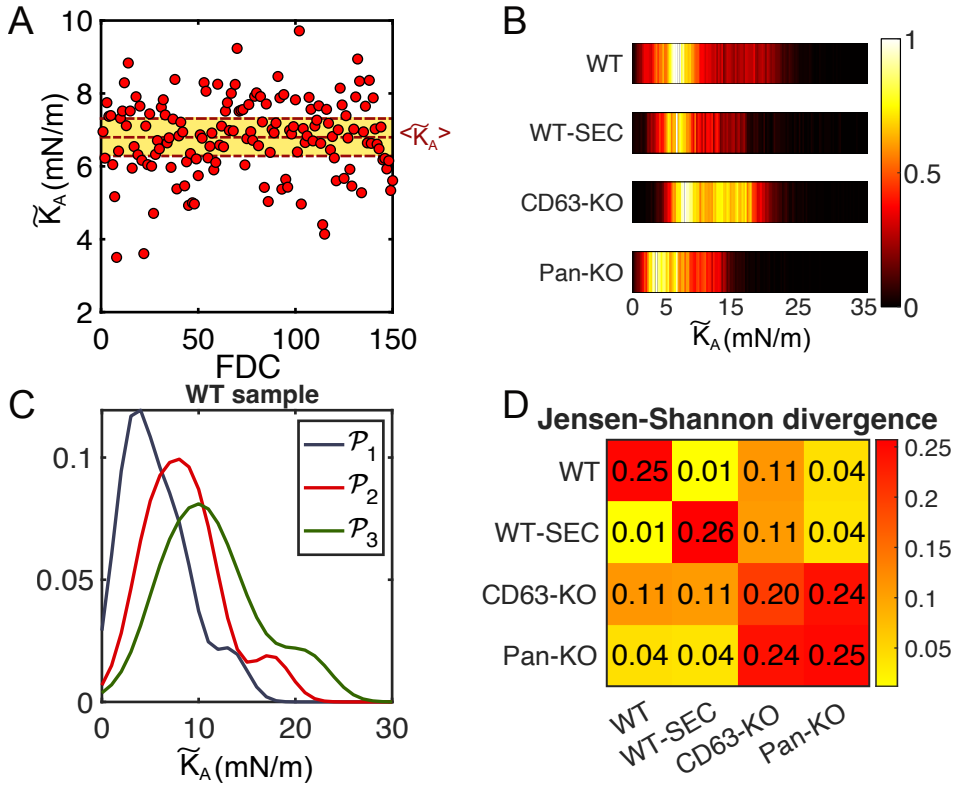


FIG. 3. **Variations of $\tilde{K}_A$ in a single vesicle**. (A) The many values of $\tilde{K}_A$ extracted from individual force–distance curve of a single vesicle. The shaded region indicates one standard deviation and the central line shows the mean value. (B) Barcode plot of all values of $\tilde{K}_A$ for all the vesicles in each family. (C) $\mathcal{P}_1$, $\mathcal{P}_2$ and $\mathcal{P}_3$ of the WT sample. (D) Jensen-Shannon divergences between effective elastic modulus of the samples. The samples are internally compared across $\mathcal{P}_1$ and $\mathcal{P}_3$ (diagonal elements) while the distance across different samples (non-diagonal elements) compares $\mathcal{P}_2$ of the two samples.

the distances is small. Note also that we find the distance between the WT family and the WT-SEC family is very small. As reported earlier [15], additional cleaning with SEC is expected to remove protein corona. Our results mean that either the effect of protein corona on $\tilde{K}_A$ is negligible or, possibly more likely, that the sample preparation steps before the AFM study which also involves several washing steps, already removes the corona. Another aspect to consider is the compositional heterogeneity of EVs derived from a cell line or even a single cell [35, 36]. Such a variation may also result in a distribution of mechanical properties as we see in our case.

### D. Measurement of bending modulus

In Fig. (4A) we show a typical example of an approach and a retraction of the AFM tip. We have already used the approach curves to find out the effective area modulus $\tilde{K}_A$. In many cases, we find that the retraction typically shows the behavior we show in Fig. (4A). This indicates the formation of a tether. In many cases of tether formation in GUVs [13, 37] and cells [38] the typical force–distance curve looks different: the force remains a (negative) constant as the length of the tether increases and eventually jumps back to zero as the tether is snapped. In such cases, minimization of the free energy gives the tether force to be $2\pi\sqrt{2\kappa\Sigma}$ where $\kappa$ is the bending modulus and $\Sigma$ is the membrane tension. Typically, this is observed in experiments in tube–pulling assays where the GUV is aspirated in a micropipette (the aspiration pressure sets the membrane tension) while a tether is pulled. Our experimental setup is different and we observe a different qualitative behavior – the force ($F$) changes as the length of the tether ($L$) increases, $F/L$ remains approximately a constant. The same behavior has already been calculated for adhered GUVs in Ref. [8]. The crucial difference between this and the tether formation in tube–pulling assays is that for the former the vesicle is not considered a quasi-infinite reservoir of lipids. This approach is appropriate for us because i) we consider adhered vesicles and ii) our vesicles are significantly smaller and thus, cannot be considered as a quasi–infinite reservoir of lipids. In general the force–distance curves obtained in Ref. [8] also depends on the adhesion forces between the vesicle and the base. By assuming the volume of the tether to be much smaller than the volume of the vesicle, following Ref. [8] we obtain a simplified

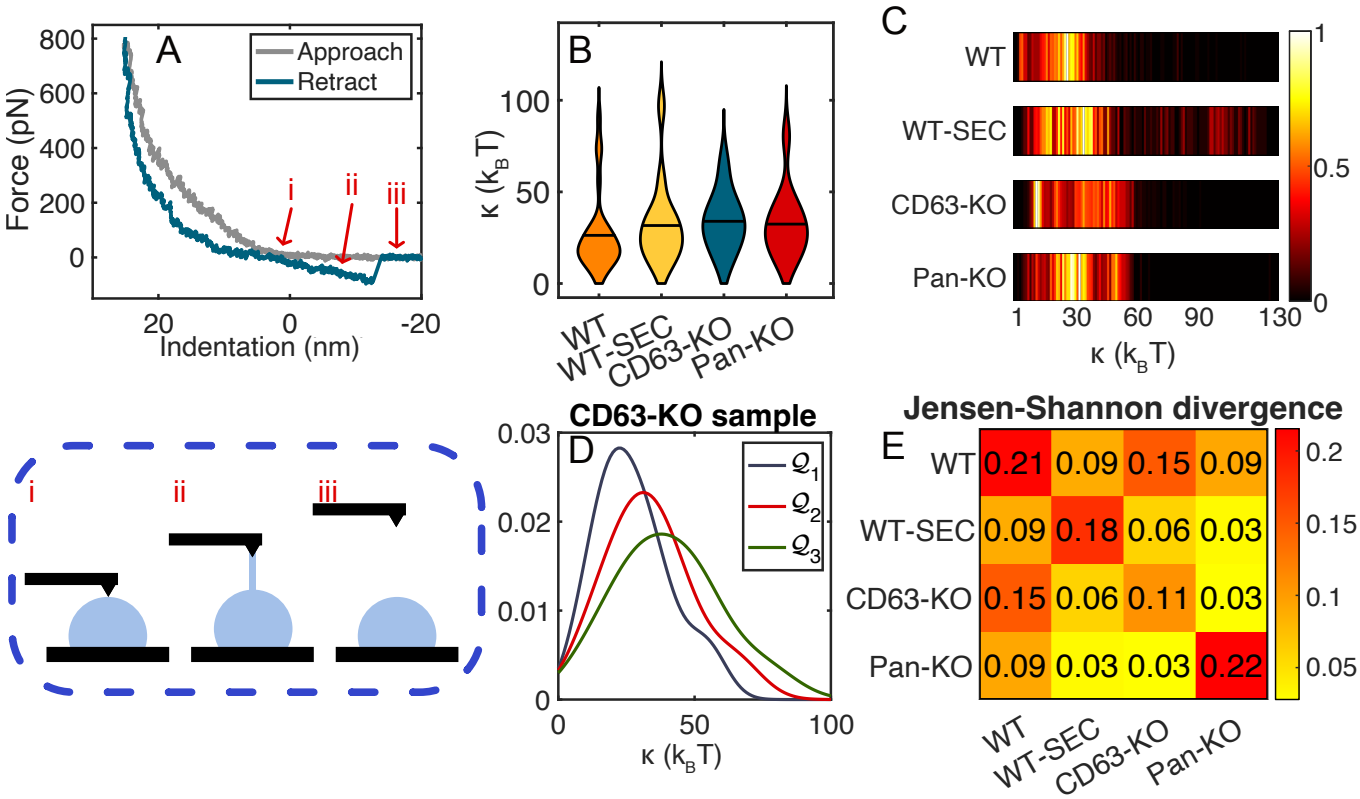


FIG. 4. **Tether formation** (A) A typical Force–distance curve with the approach (grey) and retract part (blue) which shows tether formation. The different stages of tether formation correspond to the points: (i) AFM tip touches the vesicle (ii) tip is removed, tether formed, and the area of contact between the vesicle and the substrate decreases, and (iii) tether is snapped. (B) Violin plots of the bending modulus of EVs from the WT, WT-SEC, CD63-KO, and Pan-KO families. The black line indicates the mean. (C) Normalized heatmap of all extracted bending moduli for all vesicles in each sample. Bar width: $1J/k_{\mathrm{B}}$. (D) $\mathcal{Q}_1$, $\mathcal{Q}_2$ and $\mathcal{Q}_3$ of the WT-SEC sample. (D) Jensen-Shannon divergences between effective bending modulus of the samples. The samples are internally compared across $\mathcal{Q}_1$ and $\mathcal{Q}_3$ (diagonal elements) while the distance across different samples (non-diagonal elements) compares $\mathcal{Q}_2$ of the two samples.

force–distance relation:

$$\kappa \simeq \frac{R_{\mathrm{c}} H}{4\pi}\left(1-\frac{H}{4R_{\mathrm{c}}}\right) \left[1-\left(\frac{2R_{\mathrm{c}}}{H}\right)^{\frac{1}{3}}\left(1-\frac{H}{4R_{\mathrm{c}}}\right)^{-1}\right]\left(\frac{F}{L}\right). \tag{3}$$

We use this expression to obtain the bending modulus $\kappa$ from each case of the force-distance plot involving tether formation. The PDFs of the bending modulus of the families are plotted in Fig. (4B) as violin plots. The tether formation does not happen every time the AFM tip is retracted (see discussion in IV F), therefore the sample size from which the average $\kappa$ is calculated is smaller than in the case of $\tilde{K}_{\mathrm{A}}$. Note that, similar to what happened with the measurement of $\tilde{K}_{\mathrm{A}}$, different tether formation experiment on the same vesicle yields different values for $\kappa$. In Fig. (4C) we show a barcode plot for all the bending moduli measured for different families. While the CD63-KO family and Pan-KO have a smaller spread in their values, the WT-SEC family shows a larger spread. Earlier measurements of the bending modulus in EVs have obtained values somewhere between $2-20\,\mathrm{k_B T}$ [11, 31, 32, 39]. Bending modulus of lipid bilayers in GUVs have been measured to be in the range of $10-40\,\mathrm{k_B T}$ depending on composition [40–44]. The mean values of our measurements fall in the same range although, we find several values that are somewhat larger. Once again, the PDFs of our data are not single Gaussians – they again fail the Shapiro-Wilk test (Appendix C). Hence, once again, we cannot employ the t-test to check whether the differences between different families are statistically significant. We proceed in the same way as we have done for the measurement of $\tilde{K}_{\mathrm{A}}$. The first step is to estimate the error in the measurement of $\kappa$. In (3) the bending modulus depends on the height $H$ and radius $R_{\mathrm{c}}$ of the vesicles and also the ratio $F/L$ that we obtain from the force–distance curves. We assume that the errors in measuring $H$ and $R_{\mathrm{c}}$ are small compared to the variation in $F/L$ for different cases of tether formation, i.e., we attribute

the source of error in $\kappa$ to the variation in $F/L$, i.e.,

$$\Delta\kappa \simeq \frac{R_c H}{4\pi}\left(1-\frac{H}{4R_c}\right) \left[1-\left(\frac{2R_c}{H}\right)^{\frac{1}{3}}\left(1-\frac{H}{4R_c}\right)^{-1}\right]\Delta\left(\frac{F}{L}\right), \tag{4}$$

where we obtain $\Delta(F/L)$ from the standard deviation of $F/L$ over the many measurements of tether formation. Next, we construct three PDFs for each family, one each for $\langle\kappa\rangle - \Delta\kappa, \langle\kappa\rangle$, and $\langle\kappa\rangle + \Delta\kappa$, denoted by $\mathcal{Q}_1$, $\mathcal{Q}_2$ and $\mathcal{Q}_3$. The three PDFs for the CD63-KO family are shown in Fig. (4D). We again calculate the matrix of Jensen–Shanon distances and plot them in Fig. (4E). We find again that the diagonals of this matrix are typically larger than the off-diagonal values, i.e., the difference between the families are not statistically significant. The exception is again the family CD63-KO. The distance between $\mathcal{P}_1$ and $\mathcal{P}_2$ within CD63-KO family is 0.11 whereas the distance between $\mathcal{P}_2$ of CD63-KO family with WT family is 0.15, the PDF of bending modulus of CD63-KO is (marginally) statistically distinct from the PDF of bending modulus of the WT family.

## III. DISCUSSION

Several comments are now in order.

First concerns the theoretical model that we have used to interpret the AFM measurements. We agree with earlier works [6, 11] that neither the Hertzian model nor the thin–shell–theory is appropriate to analyze the AFM measurements. We also agree that the contribution from bending is negligible. We differ from Refs. [6, 11] in one crucial way: in contrast to the main hypothesis made in these works, we assume the the volume of EVs to be constant while the area changes. We present two justifications: first, the EVs are very similar to GUVs except for their size and second, we argue that over the time scale of one force–distance measurement of very little change of volume due to the osmosis of water is possible B 3. Furthermore, a straightforward dimensional argument applied to our model reproduces the linear force–distance relationship at short distance and our detailed numerical simulations produces a good fit with the experimental data. So the first take-home lesson of our work is that the large amount of existing results on GUVs should be the best guide to understand the biomechanical properties of EVs with additional care necessary to take into account their small sizes and the fluctuations as explained next.

Second, one crucial aspect of AFM measurement of force–distance curves of EVs that we particularly emphasize are their random variations. For a *single* EV, about 150 repeated measurements give force–distance curves that are quite different from one another, see Fig. (2A). This is a peculiar aspect of EVs – never observed in GUVs to the best of our knowledge. An important point to note is that these fluctuations seem to be Gaussian and decorrelated with one another, see Fig. (3A). We identify two mechanisms that can give rise to these fluctuations.

1. **The thermal fluctuations**: Naively, we may argue that thermal effects are not important because for lipid bilayers $(k_B T/\kappa) \approx 1/20$ is less than unity. Recent theoretical works [10, 45, 46] have demonstrated that in thin shells the dimensionless number that determines the importance of thermal effects is the elasto-thermal number, given by $(k_B T/\kappa)\sqrt{Y_{2d}R^2/\kappa}$ where $Y_{2d}$ the *two-dimensional* Young's modulus. These results cannot be directly applied to EVs because EVs have a fluid membrane whereas the thin–shell theory considers a solid membrane. Nevertheless, for EVs, we can define a similar elasto-thermal number by replacing $Y_{2d}$ by $K_A$: ET $\equiv (k_B T/\kappa)\sqrt{K_A R^2/\kappa} \approx 5$, where we have used [41] $K_A \approx 200\,\mathrm{mN\,m^{-1}}$ and $\kappa \approx 10^{-19}$J, and $R = 100\,\mathrm{nm}$. The elasto-thermal number is larger than unity, hence we do expect thermal effects to be important.

2. **The diffusion of membrane molecules**: It is well known that membrane proteins diffuse on the lipid membrane [47, 48]. The diffusion constant is estimated to vary over a large range [49, Table 1]. Let us take a representative value [50] of $D \sim 1\,\mu\mathrm{m}^2\,\mathrm{s}^{-1}$. The typical time scale of a complete force–distance measurement is about 1 s. Over that time scale a protein diffuses approximately over an area of $1\,\mu\mathrm{m}^2$, which is significantly larger than the surface area of the EVs. This implies that by a single force–distance measurement, we obtain some kind of average elastic modulus. Thus every force–distance measurement yields a slightly different value of elastic modulus. However, the estimate of $D$ we have used may be inaccurate because: (i) proteins on the surface of EVs are known to form clusters [51]; (ii) the value of $D$ has been measured for almost flat surfaces [49], for example on surfaces of cells; (iii) in addition, the interaction between proteins with the AFM tip and the surface may affect their diffusion. Note also that if the characteristic time scale of diffusion of proteins slowed down so much that it became comparable to the typical time scale of a force–distance measurement, then we would expect some correlation between successive measurements. But we do not see this.

At the moment, it is not clear to us, which of these two mechanisms makes the dominant contribution. During the last couple of years, there have been several measurements of the nanomechanical properties of vesicles through atomic force microscopy [6, 30, 39, 52–55]. Most of these rest on the assumption that one or few measurements on each vesicle is enough for a representative value. Here we show explicitly and justify theoretically that this is not the case.

Third remark is about tether formation. Typical theory of force–distance curves for tether formation in GUVs [37] and cells [38] shows that the force remains a constant as the length of the tether increases and eventually jumps back to zero as the tether is snapped. Typically, this is observed in experiments in tube–pulling assays where the surface tension of the membrane is held constant. Nevertheless, the same theory has been used to interpret tether formation of adhered cells [56] and vesicles [11, 13, 19, 31] in which case the surface tension cannot be controlled. In our experiments neither can we control the surface tension – a direct consequence of adhering the vesicles – nor we can not provide excess lipids functioning as a *membrane reservoir* due to the small size of the vesicles. We obtain a linear force–distance relationship. We follow Ref [8], whose theory gives a linear force–distance relationship which we use to measure the bending modulus. To the best of our knowledge, there has been only one experimental measurement [9] of tether formation in GUVs that found a linear force–distance relationship although Ref. [9] suggested a theoretical interpretation different from Ref. [8]. The linear force–distance in tether formation is also found in bacterium [57], and fibroblasts[58] in which case the mechanism can be different. To summarise, ours is one of the first experimental observation of linear force–distance relationship which may be interpreted using the theory of Ref. [8].

Fourth, note the natural heterogeneity of biomechanical properties within a family of sEVs. Our data shows that the PDF of the elastic constant is not likely to be Gaussian but can be best represented by a superposition of several Gaussians. From the biological point of view, this is expected as EVs are known to be heterogenous containing several different subpopulations and each of them may generate a Gaussian distribution of biomechanical properties. This absence of simple Gaussianity also demands statistical methods that are suitable for families of EVs. As the underlying normality assumption for the t-test is violated we used the concept of Jensen-Shanon divergences to differentiate between probability distributions. We believe this is better suited as a statistical approach due to the natural variations of the elastic modulii of EVs.

Now let us discuss to what extent our original intention i.e. to differentiate EV subpopulations based on their elastic properties, has been served. Membrane protein-based discrimination of EV subpopulation is by far the most investigated topic in the field, thus also providing the basis for our primary question, i.e. does the elasticity of EV depend on the membrane protein composition? Tetraspanins being highly abundant in HEK293T, thus become an obvious choice for our experimental design. Note that knocking out of certain proteins may also have unwanted consequences where the proteins are replaced by other proteins or lipids. For example, it may change the cholesterol content of the EVs [59], which in turn can change their elastic properties, [see, e.g., 60, 61]. Furthermore Ref. [62] has suggested that the presence of proteins may change the local curvature of the lipid membrane thereby changing its elastic properties [62]. Our results suggest that the variation in the elastic modulus within a family is too large to detect changes in elastic modulus, induced by protein alteration, between families. The only exception is the CD63-KO sample, which shows a statistically significant difference. The final take-home message of our work is that the error in earlier experiments may have been underestimated.

Finally, nothe that another consequence of such protein diffusion is that if antibodies are used to capture the EVs, all the complementary proteins may eventually diffuse to the substrate side, thus inducing some degree of bias to the compositional fluctuations. To reduce and possibly to eliminate such a scenario, we use electrostatics capture of EVs, as we described in our previous work [63]. This approach makes the selection of sEVs less biased, as the target protein may not be equally expressed in all sEVs in a family.

Studying the nanomechanical properties of extracellular vesicles is still in the early stages. The central goal of our paper is to address one of its greatest challenges: to properly identify stable and relevant protocols of analysis of EVs.

## IV. METHODS

### A. Chemicals and materials

High-purity deionized water (DIW) with a resistivity of 18 MΩ cm was used throughout all the experiments. Casein (C5890) in powder, phosphate-buffered saline (PBS; P4417) in tablets, and poly-l-lysine (PLL; P2636) were purchased from Sigma-Aldrich (Burlington, MA, United States).

### B. Cell culture and extraction, purification, and isolation of EVs

HEK293T (human embryonic kidney-293T) cells were propagated in Dulbecco's modified Eagle's medium (DMEM) containing Glutamax-I and sodium pyruvate; 4.5 g/L Glucose; Invitrogen) supplemented with 10% fetal bovine serum (FBS; Invitrogen) and 1% Antibiotic-Antimycotic (Anti-Anti; ThermoFisher Scientific). 48 h prior to collection of conditioned media for EV isolation from HEK293T cells, cells were washed with PBS and the medium was changed to OptiMem (Invitrogen) [64]. HEK293T-HEK293T-CD63KO and -PAN-KO (CD9, CD63, and CD81) cell lines were generated by the delivery of Cas9-gRNA ribonucleoproteins (IDT, Integrated DNA Technologies, Coralville) targeting respective tetraspanin sequences using RNAiMAX (Thermo Fisher Scientific,Waltham, MA, USA). Shortly, 10,000 cells per well were seeded in a 96-well plate and treated

after 24 h with 100 ng of Cas9-RNAiMax per well, following the protocol of Chesnut et al 2015[65]. Three days after treatment the cells were stained with anti-CD63-APC or a mixture of anti-CD9/63/81-APC antibodies [14], and successfully edited cells were sorted on a BD Fusion flow cytometric cell sorter as single cells per well into 96-well plates. The resulting colonies were validated and expanded as stable cell lines. All cell lines were grown at 37°C, 5% CO2 in a humidified atmosphere and regularly tested for the presence of mycoplasma. For EV preparation, cell culture-derived conditioned media (CM) was first pre-cleared from cells and debris by low-speed centrifugation (700 × $g$ for 5 min) and subsequent centrifugation at 2,000 × $g$ for 20 min to remove larger particles and debris. Next, media was filtered through 0.22 µm bottle top vacuum filters (Corning, cellulose acetate, low protein binding) to remove any larger particles. Pre-cleared CM was subsequently concentrated via tangential flow filtration (TFF) by using the KR2i TFF system (SpectrumLabs) equipped with modified polyethersulfone (mPES) hollow fiber filters with 300 kDa membrane pore size (MidiKros, 370 $cm^2$ surface area, SpectrumLabs), at a flow rate of 100 mL/min (transmembrane pressure at 3.0 psi and shear rate at 3700 $sec^{-1}$, as described previously [66]. WT-SEC EVs were additionally purified by bind-elute size exclusion chromatography (BE-SEC): CM were concentrated by TFF as described above and then loaded onto BE-SEC columns (HiScreen Capto Core 700 column, GE Healthcare Life Sciences), connected to an ÄKTAstart chromatography system (GE Healthcare Life Sciences) as described previously [66]. Amicon Ultra-0.5 10 kDa MWCO spin-filters (Millipore) were used to concentrate the sample to a final volume of 100 µL. EVs were stored in Maxymum Recovery polypropylene 1.5 mL tubes (Axygen Maxymum Recovery, Corning, cat MCT-150-L-C) in PBS-HAT buffer (PBS, 25 mM Trehalose, 25 mM HEPES, 0.2% Human Serum Albumin) before usage as described previously [14]. Prepared sEV samples were characterized by Nanoparticle tracking analysis (NTA) to determine particle size and concentration using the NanoSight NS500 instrument equipped with NTA 2.3 analytical software and an additional 488 nm laser [66]. The samples were diluted in 0.22 µm filtered PBS to an appropriate concentration before being analyzed. At least five 30-second videos were recorded per sample in light scatter mode with a camera level of 11-13. Software settings were kept constant for all EV measurements (screen gain 10, detection threshold 7). The analysis was performed with the screen gain at 10 and the detection threshold at 7 for all EV measurements. Successful knockout of CD63 and CD9/CD63/CD81, respectively, were validated by multiplex bead-based EV flow cytometry [67] and single EV imaging flow cytometry as described before [68] (data not shown).

### C. EV sample preparation

After purification and isolation, the EVs were adhered to coverslips. The coverslips were cleaned from organic residue with a 5:1:1 RCA-1 solution of deionized water, $NH_3$, and $H_2O_2$ (90°C, 10 minutes). After cleaning, the coverslips were coated with 0.001% poly-l-lysine for 90 seconds. 100 µL of $1 \times 10^9 \frac{\text{part}}{\text{mL}}$ of the sample suspended in 1×PBS was then incubated for 1 hour at room temperature. A cut-up four-well insert (80,469, ibidi GmbH, Gräfelfing, BY, DE) was used to limit the spatial spread of the EV sample on the coverslip. After incubation, the substrate was thoroughly washed with 1×PBS. To reduce the risk of unsolved salt crystals contaminating scans, the PBS was filtered through a 0.2 µm PTFE filter (514-0070; VWR; AB, SE). Before loading the sample on the AFM, the liquid volume was increased to approximately 400 µL to avoid drying out the sample and deflating the vesicles during imaging. The dried-up sample showed up either as great spikes in the topographical image or as elongated, short vesicles, see Fig. (5) in (Appendix A).

### D. Atomic Force Microscopy (AFM)

The biophysical measurements were performed with a NanoWizard 3 BioScience AFM from Bruker (Billerica, MA, United States). A CoverslipHolder from Bruker was used to enable a liquid environment. Performing measurements in 1×PBS allows a higher preservation of their spherical shape than measurements performed in air [69]. Qp-BioAC cantilevers from NanoAndMore GMBH (Wetzlar, HE, Germany) with nominal spring constants of 0.06 N/m, 0.1 N/m, and 0.1 N/m were used. All sessions started using the cantilever with the lowest nominal spring constant which was swapped to the other cantilever as tip contamination occurred. Prior to imaging the spring constant of the cantilever was determined through the thermal noise method [70]. Images were obtained in Quantitative Image (QI) mode with an imaging force of 200 pN. First, a coarse scan of a $10 \times 10\,\mu m^2$ large region with a resolution of 39 nm/pixel was carried out. Objects with height > 25 nm and width > 100 nm at this resolution were classified as potential EVs. For this, a $500 \times 500\,nm^2$ or $400 \times 400\,nm^2$ scan centered around the object at a resolution of 3.9 or 4 nm/pixel was considered. If the object exhibited a spherical cap shape it was assumed to be a vesicle, and force spectroscopy measurements were performed at its center. The force spectroscopy measurements were carried out with the maximum indentation force of 0.8 nN. At least 150 consecutive indentations were performed at the constant speed of 1 µm/s. After the set of force spectroscopy measurements, the vesicle was imaged again to ensure that the measurements had not damaged, deformed, or otherwise moved the vesicle.

### E. Post data capture processing

In Gwyddion, all single EV images were tilt-corrected and shifted in the z-direction to let the lowest pixel represent zero level. A line profile in the slow scan direction over the EV peak was exported to Matlab where a script calculated a radius of curvature ($R_c$) by fitting a circle to all the points with heights greater than half the maximum height as previously suggested in Ref. [19]. The size of the AFM-tip, 5 nm, was taken into account by subtracting 5 nm from the radius obtained in the previous step. In the same protocol, Vorselen et al., suggest applying forces in the 5-10 nN range to completely indent the vesicle and reach the substrate. This allows the height, $H$, of the vesicle to be extracted from the force-distance curve instead of through the topographical images. However, such large forces are likely to rupture the vesicles, so we avoid this step. Instead, the height was extracted from the line profile over the center of the EV.

### F. Force distance curve analysis

The force-distance curves were processed in the JPK Data Processing program. First, the offset and the tilt of the baseline were corrected. After this, the contact point between the AFM tip and the vesicle was found. Finally, the height was corrected for cantilever bending. A successfully processed curve would have its contact point at 0 nm indentation, and a constant baseline around 0 pN. The stiffness was extracted as the slope of the approach curve in the penetration region $0.05 - 0.1$H. The retract curves were exported to Matlab where a script identified curves with tether formations and extracted their length and force magnitude. A curve would be designated with tethers if the global force minimum occurs at $< 0$ nm indentation, has a greater magnitude than 100 pN, and the force returns to the baseline before the AFM tip is returned to its original state.

### G. Statistical analysis

Statistical significance was established using an unpaired, two-sample t-test at $\alpha = 0.05$. Probability density functions were generated and compared with the Jensen-Shannon distance. All the statistical tests were scripted using MATLAB®, except for the Shapiro-Wilk goodness-of-fit test which was performed in R.

## ACKNOWLEDGMENTS

DM, VP, and VA acknowledge the financial support of the Swedish Research Council through grants 638-2013-9243 and 2016-05225. DM sincerely thanks Kheya Sengupta and Sreekanth Manikandan for the discussions. NORDITA is partially supported by NordForsk. AG is an International Society for Advancement of Cytometry (ISAC) Marylou Ingram Scholar 2019-2024 and supported by a Karolinska Institutet Network Medicine Alliance Collaborative Grant.

[1] Buzas, E. I., György, B., Nagy, G., Falus, A. & Gay, S. Emerging role of extracellular vesicles in inflammatory diseases. *Nature Reviews Rheumatology* **10**, 356–364 (2014).

[2] Hill, A. F. Extracellular vesicles and neurodegenerative diseases. *Journal of Neuroscience* **39**, 9269–9273 (2019).

[3] Hagey, D. W. *et al.* The cellular response to extracellular vesicles is dependent on their cell source and dose. *Science advances* **9** (2023).

[4] Bagci, C. *et al.* Overview of extracellular vesicle characterization techniques and introduction to combined reflectance and fluorescence confocal microscopy to distinguish extracellular vesicle subpopulations. *Neurophotonics* **9**, 021903–021903 (2022).

[5] Ma, B. *et al.* Optical imaging of single extracellular vesicles: Recent progress and prospects. *Chemical & Biomedical Imaging* (2023).

[6] Vorselen, D., MacKintosh, F. C., Roos, W. H. & Wuite, G. J. Competition between bending and internal pressure governs the mechanics of fluid nanovesicles. *ACS Nano* **11**, 2628–2636 (2017).

[7] Anselmo, A. C. & Mitragotri, S. Impact of particle elasticity on particle-based drug delivery systems. *Advanced drug delivery reviews* **108**, 51–67 (2017).

[8] Smith, A.-S., Sackmann, E. & Seifert, U. Pulling tethers from adhered vesicles. *Physical review letters* **92**, 208101 (2004).

[9] Cuvelier, D., Chiaruttini, N., Bassereau, P. & Nassoy, P. Pulling long tubes from firmly adhered vesicles. *Europhysics Letters* **71**, 1015 (2005).

[10] Paulose, J., Vliegenthart, G. A., Gompper, G. & Nelson, D. R. Fluctuating shells under pressure. *Proceedings of the National Academy of Sciences* **109**, 19551–19556 (2012).

[11] Vorselen, D. *et al.* The fluid membrane determines mechanics of erythrocyte extracellular vesicles and is softened in hereditary spherocytosis. *Nature Communications* **9**, 4960 (2018).

[12] Feng, Y. *et al.* Nanomechanical signatures of extracellular vesicles from hematologic cancer patients unraveled by atomic force microscopy for liquid biopsy. *Nano Letters* **23**, 1591–1599 (2023).

[13] Janshoff, A. Atomic force microscopy of giant unilamellar vesicles. In Dimova, R. & Marques, C. M. (eds.) *The Giant Vesicle Book*, 305–317 (CRC Press, 2019).

[14] Görgens, A. *et al.* Identification of storage conditions stabilizing extracellular vesicles preparations. *Journal of extracellular vesicles* **11**, e12238 (2022).

[15] Wolf, M. *et al.* A functional corona around extracellular vesicles enhances angiogenesis, skin regeneration and immunomodulation. *Journal of extracellular vesicles* **11**, e12207 (2022).

[16] Seifert, U. & Lipowsky, R. Adhesion of vesicles. *Physical Review A* **42**, 4768 (1990).

[17] Sengupta, K. & Limozin, L. Adhesion of soft membranes controlled by tension and interfacial polymers. *Physical review letters* **104**, 088101 (2010).

[18] Sengupta, K. & Smith, A.-S. Measuring giant unilamellar vesicle adhesion. In Dimova, R. & Marques, C. M. (eds.) *The Giant Vesicle Book*, 381–399 (CRC Press, 2019).

[19] Vorselen, D., Piontek, M. C., Roos, W. H. & Wuite, G. J. Mechanical characterization of liposomes and extracellular vesicles, a protocol. *Frontiers in molecular biosciences* **7**, 139 (2020).

[20] Théry, C. *et al.* Minimal information for studies of extracellular vesicles 2018 (misev2018): a position statement of the international society for extracellular vesicles and update of the misev2014 guidelines. *Journal of extracellular vesicles* **7**, 1535750 (2018).

[21] van der Koog, L., Gandek, T. B. & Nagelkerke, A. Liposomes and extracellular vesicles as drug delivery systems: A comparison of composition, pharmacokinetics, and functionalization. *Advanced Healthcare Materials* **11**, 2100639 (2022).

[22] Landau, L. & Lifshitz, E. *Theory of Elasticity*, vol. 7 of *Course of Theoretical Physics* (Pergamon Press Ltd., Oxford, England, 1970).

[23] Bremmell, K. E., Evans, A. & Prestidge, C. A. Deformation and nano-rheology of red blood cells: An afm investigation. *Colloids and Surfaces B: Biointerfaces* **50**, 43–48 (2006).

[24] Li, M. *et al.* Atomic force microscopy imaging and mechanical properties measurement of red blood cells and aggressive cancer cells. *Science China Life Sciences* **55**, 968–973 (2012).

[25] Sergunova, V. *et al.* Investigation of red blood cells by atomic force microscopy. *Sensors* **22** (2022).

[26] Pogorelov, A. V. *Bendings of surfaces and stability of shells*, vol. 72 (American Mathematical Soc., 1988).

[27] Roos, W., Bruinsma, R. & Wuite, G. Physical virology. *Nature physics* **6**, 733–743 (2010).

[28] Vella, D., Ajdari, A., Vaziri, A. & Boudaoud, A. The indentation of pressurized elastic shells: from polymeric capsules to yeast cells. *Journal of the Royal Society Interface* **9**, 448–455 (2012).

[29] Schäfer, E., Vache, M., Kliesch, T.-T. & Janshoff, A. Mechanical response of adherent giant liposomes to indentation with a conical afm-tip. *Soft Matter* **11**, 4487–4495 (2015).

[30] Royo, F. *et al.* Differences in the metabolite composition and mechanical properties of extracellular vesicles secreted by hepatic cellular models. *Journal of extracellular vesicles* **8**, 1575678 (2019).

[31] Sorkin, R. *et al.* Nanomechanics of extracellular vesicles reveals vesiculation pathways. *Small* **14**, 1801650 (2018).

[32] Ye, S. *et al.* Quantitative nanomechanical analysis of small extracellular vesicles for tumor malignancy indication. *Advanced Science* **8**, 2100825 (2021).

[33] Boslaugh, S. *Statistics in a nutshell: A desktop quick reference* (" O'Reilly Media, Inc.", 2012).

[34] Mehta, P. *et al.* A high-bias, low-variance introduction to machine learning for physicists. *Physics reports* **810**, 1–124 (2019).

[35] Tong, M. *et al.* Proteomic characterization of macro-, micro-and nano-extracellular vesicles derived from the same first trimester placenta: relevance for feto-maternal communication. *Human reproduction* **31**, 687–699 (2016).

[36] Lässer, C., Jang, S. C. & Lötvall, J. Subpopulations of extracellular vesicles and their therapeutic potential. *Molecular aspects of medicine* **60**, 1–14 (2018).

[37] Prevost, C., Simunovic, M. & Bassereau, P. Creating membrane nanotubes from giant unilamellar vesicles. In Dimova, R. & Marques, C. M. (eds.) *The Giant Vesicle Book*, 365–376 (CRC Press, 2019).

[38] Phillips, R., Kondev, J., Theriot, J. & Garcia, H. *Physical biology of the cell* (Garland Science, 2012).

[39] Ridolfi, A. *et al.* Afm-based high-throughput nanomechanical screening of single extracellular vesicles. *Analytical Chemistry* **92**, 10274–10282 (2020).

[40] Heinrich, V. & Waugh, R. E. A piconewton force transducer and its application to measurement of the bending stiffness of phospholipid membranes. *Annals of biomedical engineering* **24**, 595–605 (1996).

[41] Rawicz, W., Olbrich, K. C., McIntosh, T., Needham, D. & Evans, E. Effect of chain length and unsaturation on elasticity of lipid bilayers. *Biophysical journal* **79**, 328–339 (2000).

[42] Fa, N. *et al.* Decrease of elastic moduli of dopc bilayers induced by a macrolide antibiotic, azithromycin. *Biochimica et Biophysica Acta (BBA)-Biomembranes* **1768**, 1830–1838 (2007).

[43] Seto, H., Yamada, N., Nagao, M., Hishida, M. & Takeda, T. Bending modulus of lipid bilayers in a liquid-crystalline phase including an anomalous swelling regime estimated by neutron spin echo experiments. *The European Physical Journal E* **26**, 217–223 (2008).

[44] Nagle, J. F. Experimentally determined tilt and bending moduli of single-component lipid bilayers. *Chemistry and physics of lipids* **205**, 18–24 (2017).

[45] Košmrlj, A. & Nelson, D. R. Statistical mechanics of thin spherical shells. *Physical Review X* **7**, 011002 (2017).

[46] Agrawal, V., Pandey, V. & Mitra, D. Active buckling of pressurized spherical shells: Monte carlo simulation. *Physical Review E* **108**, L032601 (2023).

[47] Niemela, P. S. *et al.* Membrane proteins diffuse as dynamic complexes with lipids. *Journal of the American Chemical Society* **132**, 7574–7575 (2010).

[48] Ramadurai, S. *et al.* Lateral diffusion of membrane proteins. *Journal of the American Chemical Society* **131**, 12650–12656 (2009).

[49] Kusumi, A. *et al.* Paradigm shift of the plasma membrane concept from the two-dimensional continuum fluid to the partitioned fluid: high-speed single-molecule tracking of membrane molecules. *Annu. Rev. Biophys. Biomol. Struct.* **34**, 351–378 (2005).

[50] Vaz, W. L., Kapitza, H. G., Stuempel, J., Sackmann, E. & Jovin, T. M. Translational mobility of glycophorin in bilayer membranes of dimyristoylphosphatidylcholine. *Biochemistry* **20**, 1392–1396 (1981).

[51] McNamara, R. P. *et al.* Imaging of surface microdomains on individual extracellular vesicles in 3-d. *Journal of Extracellular Vesicles* **11**, e12191 (2022).

[52] Gazze, S. A. *et al.* High content, quantitative afm analysis of the scalable biomechanical properties of extracellular vesicles. *Nanoscale* **13**, 6129–6141 (2021).

[53] Li, S., Eghiaian, F., Sieben, C., Herrmann, A. & Schaap, I. A. Bending and puncturing the influenza lipid envelope. *Biophysical journal* **100**, 637–645 (2011).

[54] Lee, H. G. *et al.* Nanoscale biophysical properties of small extracellular vesicles from senescent cells using atomic force microscopy, surface potential microscopy, and raman spectroscopy. *Nanoscale horizons* **7**, 1488–1500 (2022).

[55] Arthur, P. *et al.* Biophysical, molecular and proteomic profiling of human retinal organoid-derived exosomes. *Pharmaceutical research* **40**, 801–816 (2023).

[56] Sun, M. *et al.* Multiple membrane tethers probed by atomic force microscopy. *Biophysical journal* **89**, 4320–4329 (2005).

[57] Jauffred, L., Callisen, T. H. & Oddershede, L. B. Viscoelastic membrane tethers extracted from escherichia coli by optical tweezers. *Biophysical journal* **93** (2007).

[58] Raucher, D. & Sheetz, M. P. Characteristics of a membrane reservoir buffering membrane tension. *Biophysical journal* **77**, 1992–2002 (1999).

[59] Palmulli, R. *et al.* Cd63 regulates cholesterol storage within endosomes and its distribution via exosomes. *Research Square* (2022).

[60] Gracia, R. S., Bezlyepkina, N., Knorr, R. L., Lipowsky, R. & Dimova, R. Effect of cholesterol on the rigidity of saturated and unsaturated membranes: fluctuation and electrodeformation analysis of giant vesicles. *Soft Matter* **6**, 1472–1482 (2010).

[61] Hofsäß, C., Lindahl, E. & Edholm, O. Molecular dynamics simulations of phospholipid bilayers with cholesterol. *Biophysical journal* **84**, 2192–2206 (2003).

[62] Rangamani, P., Mandadap, K. K. & Oster, G. Protein-induced membrane curvature alters local membrane tension. *Biophysical journal* **107**, 751–762 (2014).

[63] Stridfeldt, F. *et al.* Analyses of single extracellular vesicles from non-small lung cancer cells to reveal effects of epidermal growth factor receptor inhibitor treatments. *Talanta* **259**, 124553 (2023).

[64] Bost, J. P. *et al.* Growth media conditions influence the secretion route and release levels of engineered extracellular vesicles. *Advanced Healthcare Materials* **11**, 2101658 (2022).

[65] Liang, X. *et al.* Rapid and highly efficient mammalian cell engineering via cas9 protein transfection. *Journal of biotechnology* **208**, 44–53 (2015).

[66] Corso, G. *et al.* Reproducible and scalable purification of extracellular vesicles using combined bind-elute and size exclusion chromatography. *Scientific reports* **7**, 11561 (2017).

[67] Wiklander, O. P. *et al.* Systematic methodological evaluation of a multiplex bead-based flow cytometry assay for detection of extracellular vesicle surface signatures. *Frontiers in immunology* **9**, 1326 (2018).

[68] Görgens, A. *et al.* Optimisation of imaging flow cytometry for the analysis of single extracellular vesicles by using fluorescence-tagged vesicles as biological reference material. *Journal of extracellular vesicles* **8**, 1587567 (2019).

[69] Parisse, P. *et al.* Atomic force microscopy analysis of extracellular vesicles. *European biophysics journal* **46**, 813–820 (2017).

[70] Hutter, J. L. & Bechhoefer, J. Calibration of atomic-force microscope tips. *Review of scientific instruments* **64**, 1868–1873 (1993).

[71] Aris, R. *Vectors, tensors and the basic equations of fluid mechanics* (Courier Corporation, 2012).

[72] Bando Kiyoshi, Y. O., Kenkichi Ohba. Deformation analysis of microcapsules compressed by two rigid parallel plates. *Journal of biorheology* **27**, 18–25 (2013).

[73] Ugarte-Uribe, B., García-Sáez, A. J. & Claessens, M. M. A. E. Membrane permeability measurements. In Dimova, R. & Marques, C. M. (eds.) *The Giant Vesicle Book*, 437–451 (CRC Press, 2019).

## Appendix A: Determination of shape of EVs

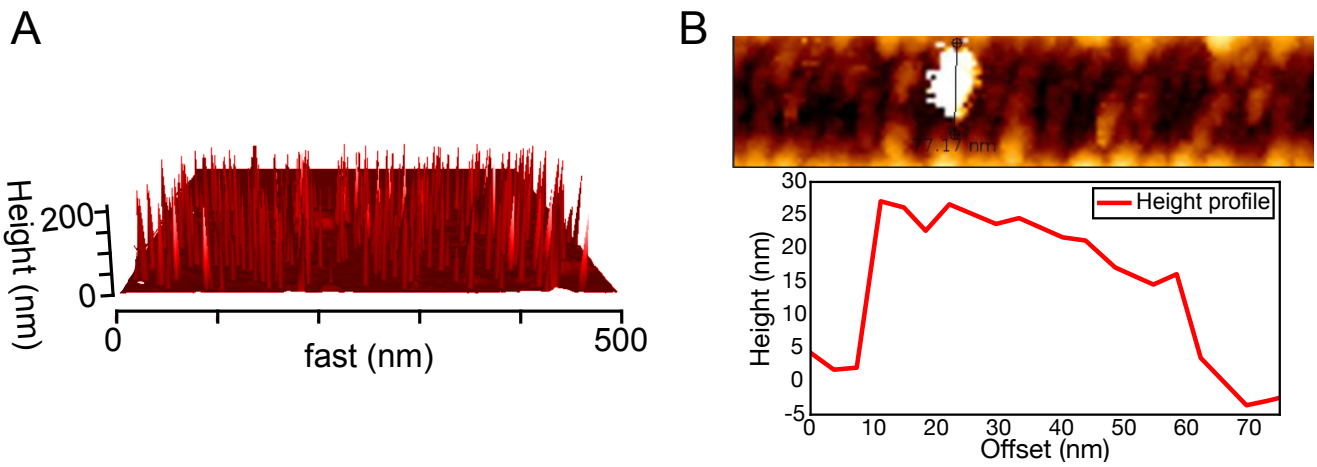


FIG. 5. **Problems caused by dried sample.** Topographical images showing (A) small height spikes and (B) a vesicle with a deflated height profile.

## Appendix B: Theory of elastic deformation of EVs

### 1. Theory for small deformation

Let us start with a vesicle adhered to a glass plate. We use a set of Cartesian coordinates $X_1, X_2, X_3$ such that the plate is given by plane $X_3 = 0$. We also introduce a generalized coordinate $x_1$ and $x_2$ the describe the surface of the vesicle [see e.g., 71]. We start with the configuration of the adhered EV on the glass surface given by the function

$$x_1 = f_1(X_1, X_2, X_3) \tag{B1a}$$
$$x_2 = f_2(X_1, X_2, X3) \tag{B1b}$$

where the functions $f_1$ and $f_2$ can be inverted to obtain

$$X_1 = F_1(x_1, x_2) \tag{B2a}$$
$$X_2 = F_2(x_1, x_2) \tag{B2b}$$
$$X_3 = F_3(x_1, x_2) \tag{B2c}$$

For example, if the undeformed shape of the vesicle where a perfect sphere just touching the glass plate, then we could use $X_1 = x, X_2 = y, X_3 = z$ where $x, y, z$ are the usual Cartesian coordinates with $z = 0$ the coordinate of the glass plate. We could use as generalized coordinates the usual angles on the surface of the sphere: $x_1 = \theta$ and $x_2 = \phi$ such that

$$\theta = \arccos\left(\frac{z}{R}\right) \tag{B3a}$$
$$\phi = \mathrm{sgn}(y) \arccos\left(\frac{x}{R^2 - z^2}\right), \tag{B3b}$$

where $R = \sqrt{x^2 + y^2 + z^2}$ is the radius of the sphere. These equations can be inverted to obtain

$$x = R\sin(\theta)\cos(\phi) \tag{B4a}$$
$$y = R\sin(\theta)\sin(\phi) \tag{B4b}$$
$$z = R\cos(\theta) \tag{B4c}$$

The deformation of the membrane relative to this configuration can be described by an in-plane (two-dimensional) vector $\boldsymbol{u}(x_1, x_2)$ and an out-of-plane (scalar) deformation $h(x_1, x_2)$. The free energy of the membrane is given by [22]

$$\mathcal{F} = \int d^2x \left[ \mu \left( s_{ij} - \frac{1}{2}\delta_{ij} s_{kk} \right)^2 + \frac{1}{2} K_{\mathrm{A}} s_{kk}^2 + \frac{1}{2}\kappa \left( \nabla^2 h \right)^2 \right] + \mathcal{F}_{\mathrm{adhesion}} \tag{B5}$$

Where $\mu$ is the in-plane shear modulus and $K_{\mathrm{A}}$ is the in-plane area modulus and $\mathcal{F}_{\mathrm{adhesion}}$ is the free energy contribution from adhesion. The area element $d^2x \equiv \sqrt{g} dx_1 dx_2$ where $g$ is the determinant of the metric tensor associated with the metric for the adhered shape. The strain tensor $s_{ij}$ is given by

$$s_{ij}(x_1, x_2) = \frac{1}{2} \left( \partial_i u_j + \partial_j u_i + \partial_i h \partial_j h \right) - \delta_{ij} \frac{h}{R_{\mathrm{v}}}, \tag{B6}$$

where $R_{\mathrm{v}}$, an effective radius of the vesicle can be set by $(4/3)\pi R_{\mathrm{v}}^3 = V$ the volume of the vesicle which is assumed to be constant. As we consider a fluid membrane we set $\mu = 0$ in (1). Let us now consider the AFM tip applying a force $F$ that causes a deformation $d$. The deformation is very small compared to the $R_{\mathrm{v}}$ such that $d/R_{\mathrm{v}}$ is a small parameter. The change in free energy can be estimated as

$$\Delta\mathcal{F} \approx R_{\mathrm{v}}^2 \left[ \frac{1}{2} K_{\mathrm{A}} \left( \frac{d^2}{R_{\mathrm{v}}^2} - \frac{d}{R_{\mathrm{v}}} \right)^2 + \kappa \frac{d^2}{R_{\mathrm{v}}^4} \right] + \Delta\mathcal{F}_{\mathrm{adhesion}} - Fd \tag{B7a}$$

$$\approx \frac{1}{2} K_{\mathrm{A}} d^2 - Fd \tag{B7b}$$

In (B7a) we assume that the gradients of the in-plane deformation to be very small and estimate the typical value of out-of-plane deformation $h$ by $d$ and the the typical derivatives of $h$ by $d/R_{\mathrm{v}}$ and the integral over the surface of the vesicle as $R_{\mathrm{v}}^2$. The last term in (B7a) is the work done on the vesicle by the AFM. It is negative because the force acts inward. To arrive at (B7b) from (B7b) we :

(a) Expand the parenthesis in (B7a) and keep only the leading order contribution in $d/R_{\mathrm{v}}$.

(b) Ignore the change in free energy of adhesion for small $d$;

(c) Ignore the contribution from bending as it is a higher order in the small parameter.

Equation (B7b) correct up to coefficients that depend on the geometry of the indentor and the adhered shape of the vesicle. Minimizing $\Delta\mathcal{F}$ with respect to $d$ we obtain $F \propto K_{\mathrm{A}} d$. Although this gives a linear force–distance relationship for small deformation this does not allow us to determine the elastic constant $K_{\mathrm{A}}$ because the constant of proportionality, which depends on the adhered shape of the vesicle and the geometry of the indentor, can not be determined by the kind of dimensional arguments given here. We need detailed numerical simulation.

### 2. Numerical simulation

In this subsection, we present our simulations of a vesicle on a substrate indented by a conical indentor to calculate the force–distance curve. This section is added for completeness. We closely follow Ref. [29, 72]. The calculation operates under the following assumptions:

1. the pressure difference across the membrane is constant,
2. Total volume is conserved, see section B 3 for justification.
3. The deformation is axially symmetric.
4. The membrane tension is uniform. a
5. Bending rigidity is negligible.

The model is shown in Fig. (6). We divide the shape into 4 regions, $\mathcal{R}_{\mathrm{i}} \equiv (s_{\mathrm{i}} \to s_{\mathrm{i}+1})$, where i goes from 1 to 4. The region $\mathcal{R}_0$ is the contact region with the flat substrate. We use Young-Laplace law:

$$\frac{\Delta P}{\Sigma} = C_1 + C_2 = \frac{d\beta}{dr} \cos\beta + \frac{1}{r} \sin\beta = \frac{du}{dr} + \frac{u}{r}, \tag{B8}$$

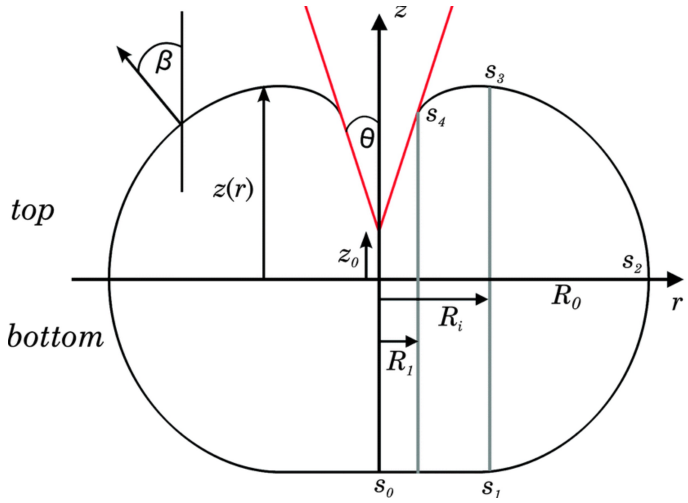


FIG. 6. Schematic of a vesicle on a substrate indented by a conical indentor. Figure reprinted with permission from [29].

where $\Delta P$ is the pressure difference across the membrane, $\Sigma$ is the tension, $C_1, C_2$ are the principal curvatures and $u \equiv \sin\beta$. Since $\Delta P/\Sigma$ is constant, we can solve Eq. (B8) for each region to get:

$$u_{\rm i}(r) = A_{\rm i} r + \frac{B_{\rm i}}{r}, \tag{B9}$$

where $A_{\rm i}, B_{\rm i}$ are the constant of integration for i-th region. We implement the following boundary conditions:

$$u = 0 \quad \text{at} \quad r = R_{\rm i} \quad , \tag{B10a}$$

$$u = 1 \quad \text{at} \quad r = R_0 \quad , \tag{B10b}$$

$$u = 0 \quad \text{at} \quad r = r(s_3) \quad , \tag{B10c}$$

$$u = -\sin\left(\frac{\pi}{2} - \theta\right) \quad \text{at} \quad r = R_1 \tag{B10d}$$

to obtain

$$A_1 = A_2 = \frac{R_0}{R_0^2 - R_{\rm i}^2}, \quad B_1 = B_2 = -A_1 R_{\rm i}^2 \tag{B11a}$$

$$A_3 = \frac{R_1 \cos\theta}{R_{\rm i}^2 - R_1^2}, \quad B_3 = -A_3 R_1^2 - R_1 \sin\left(\frac{\pi}{2} - \theta\right). \tag{B11b}$$

Right now we have three variables $R_0, R_{\rm i}$ and $R_1$ but we have two additional constraints as well. First, the force from the indentor $F_{\rm top}$ and the adhering force $F_{\rm bottom}$ should be equal. We write

$$F_{\rm top} = \pi R_1^2 \Delta P + 2\pi R_1 \cos\theta \Sigma = 2\pi \left(R_1 \cos\theta + R_1^2 A_3\right) \left(\Sigma_0 + K_{\rm A} \frac{A_{\rm ind} - A_{\rm v}}{A_{\rm v}}\right), \tag{B12a}$$

$$F_{\rm bottom} = \Delta P \pi R_{\rm i}^2 = 2\pi R_{\rm i}^2 A_1 \left(\Sigma_0 + K_{\rm A} \frac{A_{\rm ind} - A_{\rm v}}{A_{\rm v}}\right), \tag{B12b}$$

where $\Sigma_0$ is the pre-tension, i.e., tension before indenting. This is an effective parameter to take into account the fact that before indenting the vesicle is adhered to the surface and not a perfect sphere. The area before indentation is $A_{\rm v}$ and

$$A_{\rm ind} = \pi R_i^2 + 4\pi \int_{R_{\rm i}}^{R_0} \frac{r}{1 - u_1^2(r)} dr + 2\pi \int_{R_1}^{R_{\rm i}} \frac{r}{1 - u_3^2(r)} dr + \frac{\pi R_1^2}{\sin\theta} \tag{B13}$$

is the area of the vesicle after indentation. By setting $F_{\rm top} = F_{\rm bottom}$, we get

$$R_{\rm i} = \sqrt{\frac{R_0^2 R_1 \cos\theta + R_0 R_1^2}{R_0 + R_1 \cos\theta}}. \tag{B14}$$

Additionally, the volume of the vesicle

$$V_{\rm ind} = 2\pi \int_{R_{\rm i}}^{R_0} \frac{u_1^2(r) r^2}{\sqrt{1-u_1^2(r)}} dr - \pi R_{\rm i}^2 \int_{R_{\rm i}}^{R_0} \frac{u_1(r)}{\sqrt{1-u_1^2(r)}} dr + \pi \int_{R_1}^{R_{\rm i}} \frac{u_3^2(r)}{\sqrt{1-u_3^2(r) dr}} - \pi \frac{R_1^3}{3\tan\theta} \tag{B15}$$

is also conserved. We satisfy this constraint numerically. The indentation depth, d, in terms of $R_0, R_{\rm i}$ and $R_1$ is

$$d = 2R_{\rm v} - \int_{R_{\rm i}}^{R_0} \frac{u_1(r)}{\sqrt{1-u_1^2(r)}} dr - \int_{R_1}^{R_{\rm i}} \frac{u_3(r)}{\sqrt{1-u_3^2(r)}} dr + \frac{R_1}{\tan\theta}, \tag{B16}$$

where $R_{\rm v}$ is the radius of the vesicle before deformation. We start with some values of $R_0$, and use constraint in (B15) and (B14) to compute the vesicle shapes for different indentations. We compute $d$ and $F$ using (B16) and (B12b) respectively. Thus we get a force-distance curve for a given $K_{\rm A}$ and $\Sigma_0$. We then choose $K_{\rm A}$ and $\Sigma_0$ such that it minimize the distance between the least–square distance numerical and experimental curve. Since the force values range in three decades, we optimize the logarithmic mean square error. A representative example is shown in Fig. 2(B) and (C) in the main text.

### 3. Are the deformations volume conserving?

Let us try to estimate how well volume conservation is satisfied. The bilipid membrane is permeable to water with a permeability coefficient $p_{\rm w}$ which varies from about 10 to $100 \times 10^{-6}$ m/s in bilipid vesicles [73]. The flux of water molecules is given by

$$J = p_{\rm w} \left(c_{\rm in} - c_{\rm out}\right) \tag{B17}$$

where $c_{\rm in}$ and $c_{\rm out}$ are the density of water inside and outside the vesicle, respectively. Before the deformation there is no flux, the vesicle is in equilibrium and $c_{\rm in} = c_{\rm out} = N/V$, where $N$ is the number of water molecules inside and $V$ is the volume of the vesicle. Now we consider a case where the tip of the AFM moves by a distance $d$ in time $\Delta t$. The corresponding change in volume is $\Delta V \propto d^3$. The density of water outside remains the same. The density of water inside increases to

$$c'_{\rm in} = \frac{N}{V - \Delta V} \tag{B18}$$

This difference in density drives a flux as given in (B17). The total number of molecules that leave the volume is given by

$$\Delta N = J A \Delta t \tag{B19}$$

where $A$ is the area of the vesicle. We obtain

$$\frac{\Delta N}{N} = p_{\rm w} A \Delta t \frac{1}{N} \left(c'_{\rm in} - c_{\rm out}\right) \tag{B20a}$$

$$= p_{\rm w} A \Delta t \left(\frac{1}{V - \Delta V} - \frac{1}{V}\right) \tag{B20b}$$

$$= p_{\rm w} \frac{A}{V} \Delta t \left(\frac{1}{1 - (\Delta V/V)} - 1\right) \tag{B20c}$$

$$\approx p_{\rm w} \frac{A}{V} \Delta t \left(\frac{\Delta V}{V}\right) \tag{B20d}$$

$$\approx 10^{-2} \frac{\Delta t}{\rm s} \tag{B20e}$$

Here we have used $p_{\rm w} \approx 1 \times 10^{-6}\,{\rm m\,s^{-1}}$, $R_{\rm v} \approx 100\,{\rm nm}$, and $(\Delta V/V) \sim (d/R_{\rm v})^3$ with $d/R_{\rm v} \approx 1/10$. Here we have used $A \sim R_{\rm v}^2$, $V \sim R_{\rm v}^3$ and $d/R_{\rm v} \approx (1/10)$ which is certainly true for small deformation. For GUVs $d/R_{\rm v}$ lies approximately in the same range as shown in Figure 12.3 in Ref. [13].

## Appendix C: Shapiro-Wilk test

TABLE I. Shapiro-Wilk goodness-of-fit test. Resulting p-values from the Shapiro-Wilk test for the different samples and the two calculated mechanical properties. $H_0$ = The data is from a normal distribution.

| P-value | WT | WT-SEC | CD63-KO | Pan-KO |
|---|---|---|---|---|
| Linear stiffness | 0.00 | 0.24 | 0.17 | 0.36 |
| Bending modulus | 0.00 | 0.00 | 0.80 | 0.07 |

## Appendix D: Force distance curves (FDC)

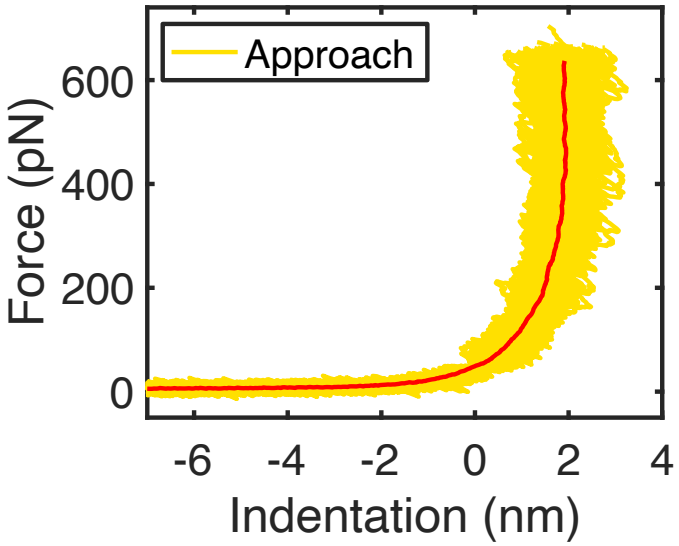


FIG. 7. **FDC on the substrate.** 150 FDC superpositioned on each other to show the spread of curves. The average force–distance curve is shown in red. The superposition is set so each curve has a zero indentation at 50 pN

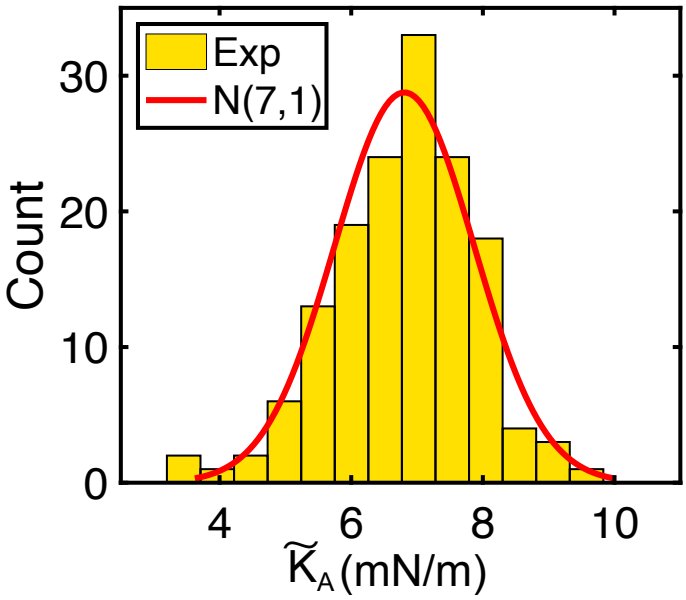


FIG. 8. **Normality of $\tilde{K}_A$ within one vesicle.** Histogram plot of 150 extracted $\tilde{K}_A$ on a single vesicle. A fitted normal distribution is shown in red.

### Appendix E: PDF of effective elastic modulus

The PDFs were estimated with kernel smoothing function estimate between $0 - 30$ mN/m.

TABLE II. **Bandwidth**. Bandwidth of the generated PDFs in Fig. 9. Selected with Silverman's rule of thumb.

| Bandwidth | $\mathcal{P}_1$ | $\mathcal{P}_2$ | $\mathcal{P}_3$ |
|---|---|---|---|
| WT | 1.56 | 1.89 | 2.27 |
| WT-SEC | 1.24 | 1.98 | 2.63 |
| CD63-KO | 1.80 | 2.12 | 2.33 |
| Pan-KO | 2.24 | 2.55 | 3.41 |

TABLE III. **Area under curve**. Area under the $\tilde{K}_A$ probability density functions from the kernel density estimator. The value of 1 indicates a proper probability density function.

| | $\tilde{K}_A - \Delta\tilde{K}_A$ | $\tilde{K}_A$ | $\tilde{K}_A + \Delta\tilde{K}_A$ |
|---|---|---|---|
| WT | 0.9714 | 0.9926 | 0.9952 |
| WT-SEC | 0.9922 | 0.9906 | 0.9854 |
| CD63-KO | 0.9977 | 0.9987 | 0.9952 |
| Pan-KO | 0.9376 | 0.9840 | 0.9945 |

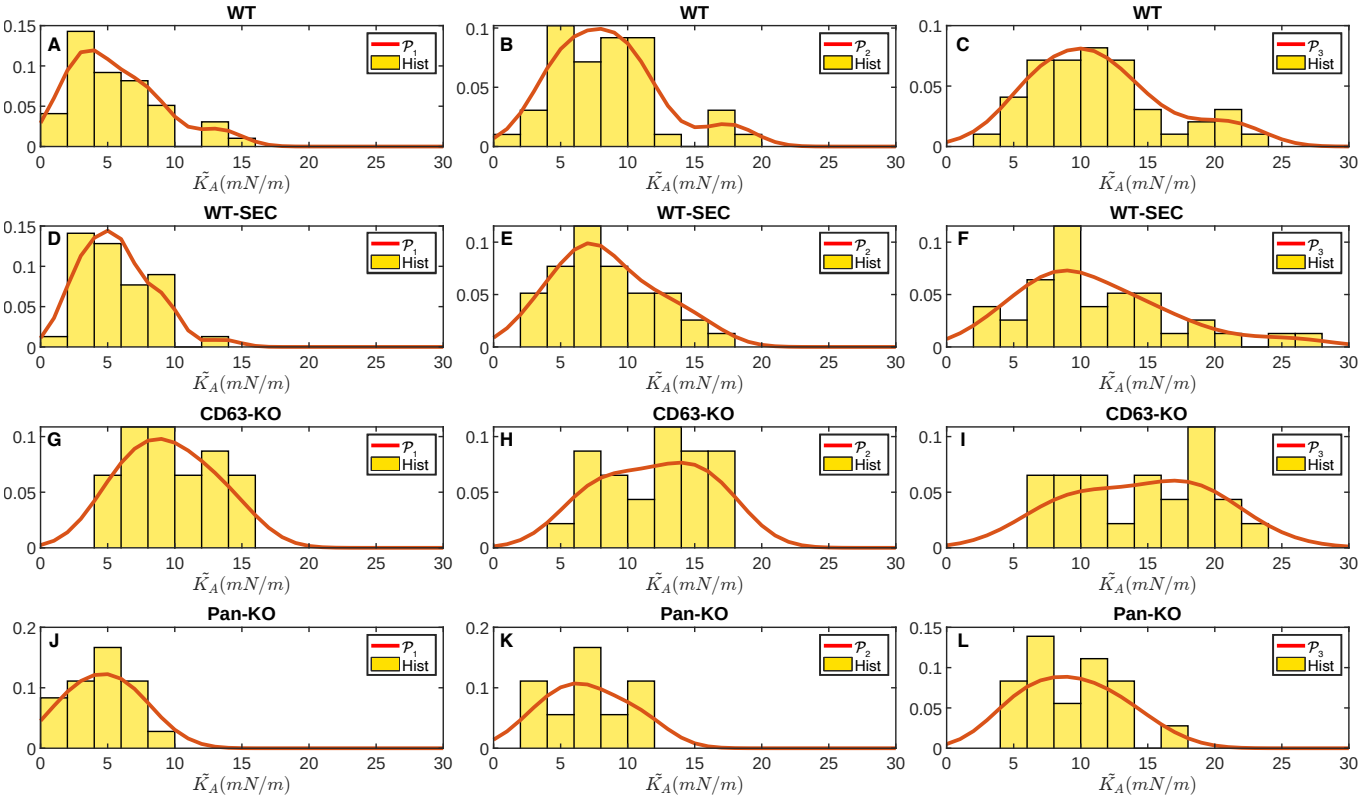


FIG. 9. **Effective elastic modulus.** Histogram of linear stiffnesses and their corresponding probability density function. Each row corresponds to a specific sample and each column a way to achieve the linear stiffness values. (A-C) show the histogram and pdf for the WT sample, (D-F) WT-SEC, (G-I) CD63-KO, and (J-K) for Pan-KO. Probability density functions generated with kernel smoothing function estimate.

## Appendix F: PDF of bending modulus

TABLE IV. **Bandwidth**. Bandwidth of the generated PDFs in Fig. 10. Selected with Silverman's rule of thumb.

| Bandwidth | | | |
|---|---|---|---|
| WT | 4.34 | 6.20 | 7.49 |
| WT-SEC | 6.02 | 7.89 | 9.18 |
| CD63-KO | 8.49 | 9.04 | 9.40 |
| Pan-KO | 6.98 | 9.24 | 11.29 |

TABLE V. **Area under curve.** Area under the generated bending modulus probability density functions from the kernel density estimator. The value of 1 indicates a proper probability density function.

| | $\kappa - \Delta\kappa$ | $\kappa$ | $\kappa + \Delta\kappa$ |
|---|---|---|---|
| WT | 0.9670 | 0.9771 | 0.9801 |
| WT-SEC | 0.9666 | 0.9792 | 0.9648 |
| CD63-KO | 0.9871 | 0.9827 | 0.9800 |
| Pan-KO | 0.9478 | 0.9812 | 0.9741 |

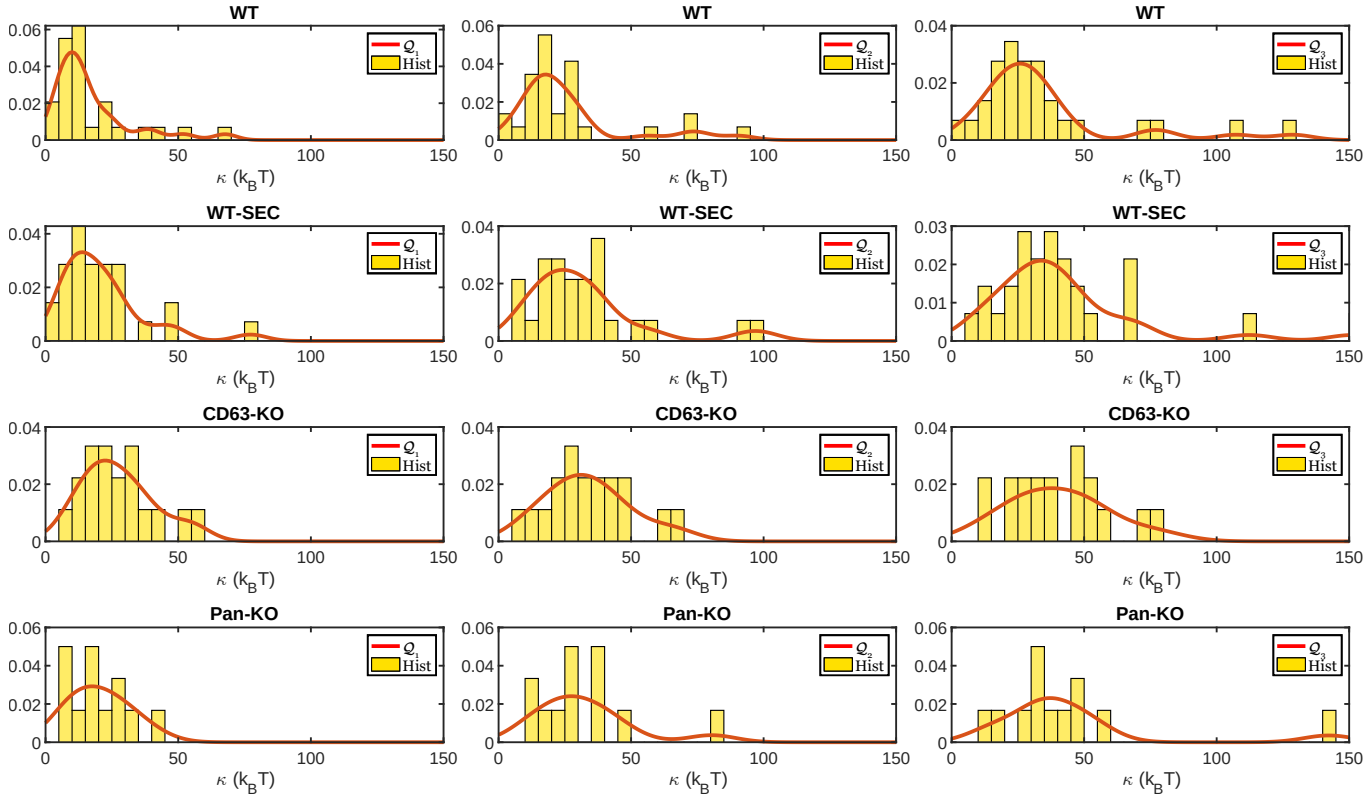


FIG. 10. **Bending modulus.** Histogram of bending modulus and their corresponding probability density function. Each row corresponds to a specific sample and each column a way to achieve the linear stiffness values. (A-C) show the histogram and pdf for the WT sample, (D-F) WT-SEC, (G-I) CD63-KO, and (J-K) for Pan-KO. Probability density functions generated with kernel smoothing function estimate with positive support and bandwidth = 0.5.

## Appendix G: Force curve rejection

Not all force curves obtained from the indentation measurements were used in the analysis. Some force curves were disqualified due to measurement errors. This could be determined by the approach and retrace baselines not being constant, or not overlapping far away from the vesicle, or from unusually high noise levels. If the approach baseline is not constant the contact point can not be determined correctly, leading to erroneous intervals for determining $\tilde{K}_{\mathrm{A}}$. During measurements, there is a risk of the AFM drifting or the vesicle moving. Because of this, force curves presumably taken on a vesicle but showing very stiff behavior were ignored and assumed to have been recorded on the substrate.

Force curves showing jump-in behavior in the approach–part were also ignored, since this is not a physical behavior for the tip-membrane interaction. The reason for the jump-in behavior in the force curves is unknown to us. A membrane tether was considered to have formed if a linear attractive force was detected in the retrace curve with a jump-back to the baseline past the contact point. Some vesicles ended up with no tethers good enough for consideration. While these vesicles were discarded in the extraction of the bending modulus, the corresponding approach curves were still considered when determining $\tilde{K}_{\mathrm{A}}$.